

DOI: 10.1002/adem.200700063

Reconstructing a Nanoporous Metal in Three Dimensions: An Electron Tomography Study of Dealloyed Gold Leaf**

By H. Rösner,* S. Parida, D. Kramer, C. A. Volkert and J. Weissmüller

Dealloying is a chemically or electrochemically driven corrosion process in which the less noble component of an alloy is selectively removed.^[1–4] It has been used to produce monolithic metal bodies with a bi-continuous structure in which two phases, solid ligaments and pore space, interpenetrate at a characteristic length scale of a few nanometres. Ag-Au alloys form a model system for dealloying, since the continuous solid solubility and the very small difference in the atomic volumes of the constituents allow for an essentially coherent transformation from the master alloy to the nanoporous gold product structure. Recently, as nanoporous gold has become of interest for possible application as a low-temperature heat exchanger,^[5] catalyst or catalyst support,^[6] or actuator material,^[7] studies of dealloying have turned from understanding corrosion towards learning how to make porous nanomaterials for functional or structural applications. Concurrent with this trend is an emerging need for detailed characterization of materials science aspects of nanoporous gold. The defect structure of the material is the subject of ongoing research.^[8]

Furthermore, first data on mechanical performance are becoming available, testifying to astonishing properties on a nanoscale level.^[9,10] However, little quantitative information is available on the central microstructural and topological properties which characterize porous structures, such as specific surface area, distribution of pore- and ligament sizes, network connectivity, and structural anisotropy. Besides the freshness of the issue, the very smallness of the structures, often well below the 10 nm size range, has prevented detailed studies so far. Here, we present a study of the nanoporous gold microstructure using electron tomography in a transmission electron microscope (TEM).

Electron tomography is a technique which provides three dimensional (3-D) information on a nanometre scale,^[11,12] and which has recently been extended beyond applications in life sciences towards the characterization of 3-D structures in materials science.^[13–18] High-angle annular dark-field scanning transmission electron microscopy (HAADF-STEM) imaging is based on Z-contrast due to Rutherford scattering,^[12,17] where the intensity scales with the atomic number ($Z^{-1.7}$) and the projected sample thickness.^[12] Therefore HAADF-STEM imaging is well-suited for electron tomography of crystalline materials^[12,19] since the contrast does not suffer from diffraction effects except when the observation area is imaged along a major zone axis. Since major zone axes are rarely encountered during the acquisition of tilt series, the overall effect on 3-D reconstructions is small.^[12] However, limits to the resolution of the reconstructed volume are imposed by the restricted tilt range (missing wedge problem), which results from the pole piece/sample holder geometry.

In this article we have applied HAADF-STEM imaging for electron tomography to characterize the 3-D structures of dealloyed white gold leaf. As was pointed out recently by Erlebacher and coworkers,^[20] this material provides a convenient model material for studies of nanoporous gold synthesis and structure, and it has the added advantage that the roughly 100 nm thick leaf samples provide electron transparent nanoporous gold that can be investigated by TEM without further preparation.^[8] The 3-D reconstructions obtained by TEM are stereographically analysed^[21,22] to yield numbers for porosity and characteristic ligament and pore sizes.

Experimental Details

Nanoporous gold has been prepared by dealloying as-received 6 carat white gold leaf^[8,20] purchased from Wasner Blattgold GmbH (Schwabach, Germany). From the weight

[*] Dr. H. Rösner, S. Parida, Dr. D. Kramer,
Priv.-Doz. Dr. J. Weissmüller^[+]
Forschungszentrum Karlsruhe GmbH in der Helmholtz-
Gemeinschaft
Institut für Nanotechnologie
Postfach 3640, D-76021 Karlsruhe, Germany
E-mail: harald.rosner@int.fzk.de

Dr. C. A. Volkert
Forschungszentrum Karlsruhe GmbH in der Helmholtz-
Gemeinschaft
Institut für Materialforschung II
Postfach 3640, D-76021 Karlsruhe, Germany

[+] also with:
Universität des Saarlandes
Technische Physik, Saarbrücken, Germany

[**] Support by the Deutsche Forschungsgemeinschaft (Centre for Functional Nanostructures Karlsruhe) is gratefully acknowledged. Dr K. Schladitz at Fraunhofer Institut für Techno- und Wirtschaftsmathematik (IFWM), Kaiserslautern, Germany, is thanked for discussions and the stereological analysis using MAVI. Dr C. Kübel at Fraunhofer Institute for Manufacturing Technology and Applied Materials Research (IFAM), Bremen, is thanked for valuable discussions regarding the 3-D reconstructions using Inspect 3D and Amira.

per area of the as-received foils their average thickness was estimated to be 120 nm. Energy-dispersive x-ray (EDX) fluorescence data indicates a composition of $\text{Ag}_{80}\text{Au}_{20}$. TEM samples were prepared from 1 cm² sample pieces which were electrochemically dealloyed in perchloric acid (1 M) at ambient temperature and at a controlled potential of 600 mV versus a $\text{Ag}/\text{AgCl}/\text{HClO}_4$ reference electrode. The dealloying potential was applied until the current fell to below 1 $\mu\text{A}/\text{cm}^2$. As described in Ref.,^[8] the comparatively low dealloying potential results in a very slow dissolution – here, the process took about 90 min. – and in a comparatively large structure size. Investigations of structure size by electron microscopy or of specific surface area by capacitance measurements typically show that significant coarsening occurs during synthesis. Thus, the structure observed here is most likely the product of two processes, corrosion and coarsening.

HAADF-STEM tomography has been carried out in a FEI Tecnai F20ST field-emission gun (FEG)-TEM operated at 200 kV, fitted with a Fischione HAADF detector (model FP-5360/20). Single-axis tilt series were acquired automatically using the Xplore3D 2.0 Tomography suite operated in the HAADF-STEM mode with a nominal spot size of 1 nm. A camera length of 70 mm (corresponding to a minimum scattering angle of 50 mrad) was used for the signal collection in order to minimise diffraction effects. Images were scanned with 1024 × 1024 pixels using a frame time of 12.5 s. 73 electron micrographs have been collected over a tilt range of $\pm 66^\circ$ in 1.8° steps. Re-centering and refocusing were done automatically. The alignment of the individual stacks and the reconstruction of the acquired tilt series was done off-line using FEI's software package Inspect 3D Version 2.1. The tilt series alignment was made by iterative cross-correlations to sub-pixel accuracy. The aligned tilt series was reconstructed

using the iterative back-projection process SIRT^[23] which is implemented in the Inspect 3D Code. 25 iterations were performed for the SIRT reconstruction. Each three-dimensional pixel ('voxel') of the reconstruction represents a cube with an edge-length of 0.73 nm. The software package Amira 3.1 has been used for the visualization of the reconstructed structures.

For stereological analysis, the reconstruction was binarized and then cropped in all spatial directions (to 340 nm × 300 nm × 70 nm) in order to remove the macroscopic sample surfaces, to avoid artefacts at the borders of the reconstruction, and to ensure that the volume used for analysis is representative of the bulk sample structure. The analysis was performed using the program MAVI.^[21] MAVI affords a characterization of 3-D structures by analysis of their representations as binary and spatially discrete images, using the algorithms described in reference [22].

Results of Electron Microscopy

Conventional TEM micrographs, such as the bright-field micrographs of Figure 1, are 2-D projections which reveal information about the average density along the beam direction. Here, the micrographs illustrate the typical microstructure of nanoporous gold, which is composed of nanometer size ligaments and pores. Energy dispersive analysis of X-ray fluorescence of the sample volume shown in Figure 1(a) indicates that the average composition is $\text{Au}_{96}\text{Ag}_4$. Details of individual gold ligaments are shown in Figure 1(b).

A selected area electron diffraction (SAED) pattern (the aperture corresponds to a circular area of about 800 nm in diameter) from the same volume as shown in Figure 1(a) (see inset) reveals a preferred $\langle 100 \rangle$ out-of-plane orientation, con-

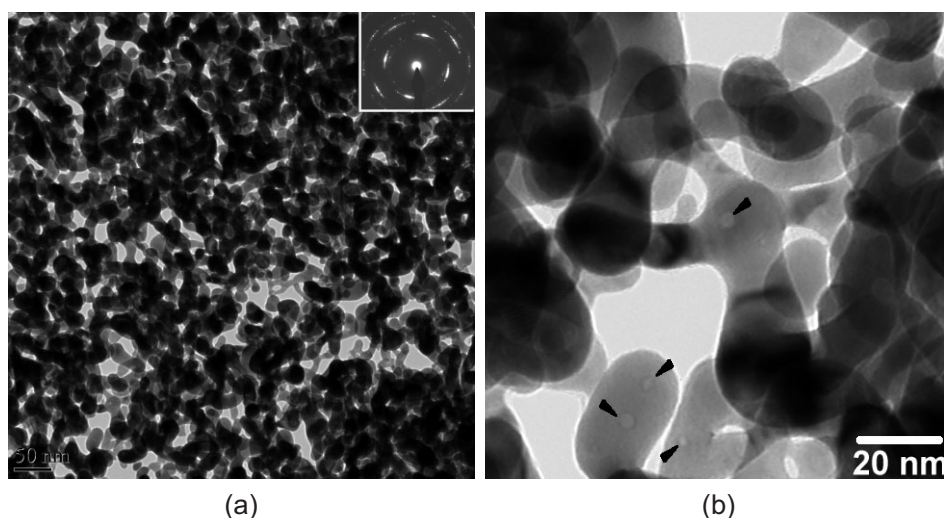


Fig. 1. a) Bright-Field micrograph showing a fully connected network structure composed of single-crystalline gold ligaments and pores. Darker regions are related to a higher density of gold ligaments due to the overlap in the 2-D projection. The corresponding diffraction pattern (SAED) in the inset indicates a preferred $\langle 100 \rangle$ out-of-plane orientation with considerable mosaic spread. b) Bright-Field micrograph: detail revealing individual gold ligaments. Examples of encased voids are marked by arrow heads.

sistent with the strong out-of-plane $\langle 100 \rangle$ texture found in an x-ray texture analysis.^[24] This is the same texture as the fully dense white gold leaf and supports the idea that the crystal microstructure has not been dramatically changed by dealloying. The presence of discrete diffraction maxima in the SAED pattern indicates that the observation area is essentially a coherent crystalline region. However, the azimuthal width and granularity of the peaks indicate significant spread in crystal orientation in the sampled volume, indicating the presence of strain inhomogeneities and/or lattice defects, in agreement with the findings in reference [8].

A noteworthy observation is the presence of numerous voids – appearing spherical and with diameters ranging from 1 to 5 nm – situated within the ligaments, as indicated by arrows in Figure 1(b). These voids are also observed in the 3-D reconstruction of the sample. It is emphasized that a dedicated TEM-inspection of the as-received gold leaf gave no evidence for any significant porosity. Thus, the pores must have formed during the dealloying process.

Although much can be learned from the micrographs shown in Figure 1, they are not sufficient to determine the ligament and pore shapes and sizes and especially their degree of interconnection. For an accurate determination of these parameters, a 3-D reconstruction is required. We have chosen a region which was thin enough to acquire tilt series of good image quality, and which appeared – in conventional bright-field microscopy – representative based on a comparison with numerous investigations on similar nanoporous gold samples.

Different views of the 3-D density distribution of a $350 \text{ nm} \times 300 \text{ nm} \times 200 \text{ nm}$ volume of nanoporous gold leaf reconstructed from HAADF-STEM tomography are displayed in Figures 2(a,b). Among the obvious features in Figure 2(a) are the high connectivity as well as the large variation in ligament and pore size. The cross-sectional view of the reconstruction in Figure 2(b) illustrates the planar charac-

ter of the sample surfaces, and shows that the leaf is around 90 nm thick at this location. The thickness of the leaf varied from position to position and the thinnest regions were chosen for the analysis.

An inspection of individual slices through the reconstructed volume (Fig. 3) allows the porous structure to be analysed in more detail. The slices have a thickness of a single voxel, so that the brightness in the images is linearly related to the reconstructed density. Since the actual density of the gold ligaments may certainly be identified with that of crystalline gold, the variations in brightness shown in the images must reflect smearing of the actual structure by the reconstruction process. Despite this blurring – which is at a length scale of around 1 nm – many aspects of the 3-D structure are revealed.

As mentioned above, enclosed voids within ligaments are abundant in the reconstruction, as indicated by arrows in Figure 3. As compared to the size of the interconnected pores, the voids are much smaller, of the order of 1–5 nm. Since the encased pores are also apparent in the non-reconstructed images, they cannot be a reconstruction artefact.

Analysis and Discussion

In order to better visualize the microstructure, and as a prerequisite for 3-D stereological analysis, the 3-D reconstruction was binarized. Surface renderings of the binarized structure are shown Figure 4. The threshold value for binarization was determined by careful comparison between slices of the binarized structure and the reconstructed densities (Fig. 3) and by requiring that there be no ‘free-floating’ gold segments.

Figure 4(a) illustrates that the structure is quite non-uniform: the diameter of the ligaments varies from less than 5 nm for the thinnest bridges to more than 30 nm for the thickest bulges, which occur mainly in the interior of the sam-

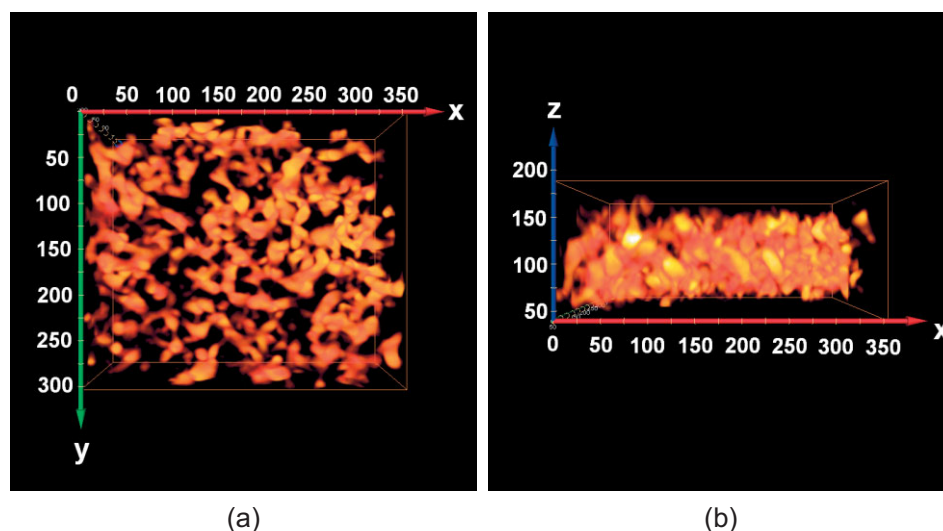


Fig. 2. Rendered volume showing the 3-D structure of the dealloyed gold leaf sample. a) X-Y (in-plane) view. Axis labels give position in nm. b) X-Z view of the inspected volume.

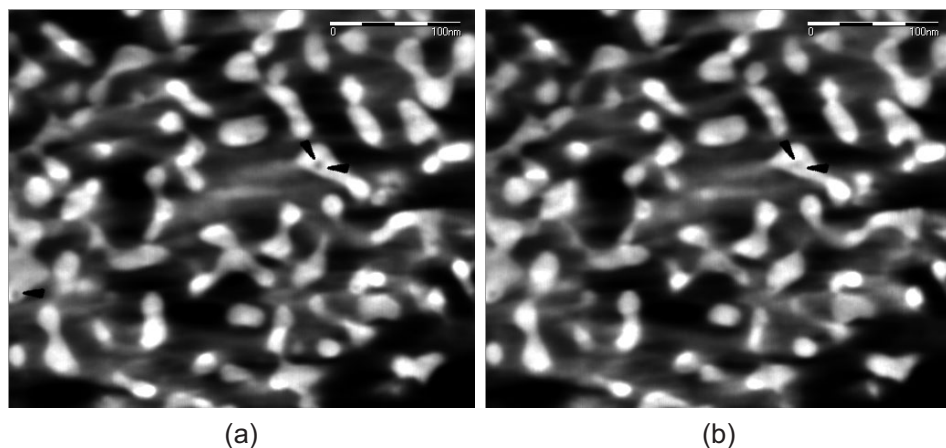


Fig. 3. Two neighbouring X-Y slices through the reconstructed nanoporous gold volume. The brightness scales with the reconstructed local density. Arrows indicate voids inside the ligaments.

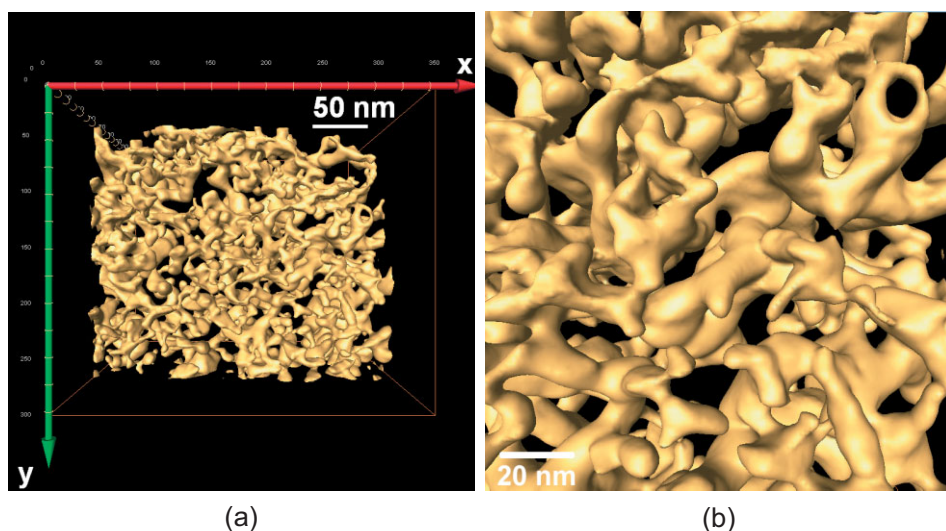


Fig. 4. a) Surface rendering of the solid phase in the binarized, reconstructed image of nanoporous gold leaf. The macroscopic sample geometry is a sheet, and the x- and y-coordinates in the figure are in-plane. b) Detail of (a). View into the bulk with one of the sample surfaces in the foreground. c) Detail of (a). A volume element cut from the bulk, viewed from different directions. Note the complex topology of the ligaments. Sheet normal is along the vertical edges of the bounding boxes. Horizontal edges are 150 nm long.

ple. The wide range in pore sizes is another aspect of structural diversity. Figure 4(b) shows that small pores and small, almost circular ligament rings coexist with much larger and quite complex pores and rings.

Although part of the relevant literature^[10,25,26] refers to nanoporous metals made by dealloying as ‘foams’, the images do not show what we would typically associate with that type of porous material. Most notably, one cannot natu-

rally identify distinct cells in the pore phase, nor do the ligaments resemble remnants of cell walls or triple lines. The configuration shown in Figure 4(c) may serve to illustrate the complex topology. One may see regions where three, four, or even five ligaments meet each other. However, the junctions do not typically appear as clearly formed nodes, and in many instances we did not find it obvious how to discriminate between, for instance, two closely spaced bifurcations and a single, four-coordinated node. Thus, without first skeletonizing the structure, there is no obvious way to estimate the characteristic number of ligaments connected in a node.

'Dead end' ligaments, that is, unconnected protrusions which are at least as long as they are wide, are found mostly at the surface of the sample. The small number of 'dead ends' within the bulk of the structure is remarkable for the following reason: the synthesis of the porous structure involves considerable coarsening,^[8] resulting in a reduction of surface area, increase of the characteristic structure size, and decrease of the number of ligaments per volume. The fundamental process would seem to be curvature-driven diffusion, with redistribution of matter away from the thinnest ligaments and towards the thickest nodes. This is similar to a Plateau-Rayleigh instability:^[27] cylinders with surface tension are unstable when their aspect ratio (length over diameter) exceeds the value of π . Here, this results in pinch-off of thin ligaments, and hence in the formation of 'dead ends'. Apparently, these 'dead ends' vanish quickly (which would be in keeping with their small size and large mean curvature), so that few of them are observed at any given time.

The observation of closed pores or voids of about 1–5 nm size within the ligaments is unexpected: alloy corrosion, which presupposes open porosity for access of the electrolyte to the corrosion front, is not expected to directly create closed pores. It is also not obvious how ligament coarsening can result in porosity, since the fundamental process – as discussed above – would seem to widen existing pores rather than create new ones. It is conceivable that the voids are created by the aggregation of lattice vacancies, but the origin of these defects remains puzzling. The injection of excess vacancies at the corrosion front under any conditions is controversial,^[28,29] and it appears particularly unlikely here since the corrosion potential was small, so that only a low superficial vacancy supersaturation can be expected. Dislocation reactions might also create vacancies, but few lattice dislocations are found at the small dissolution potential used here.^[8]

Stereological analysis of a volume cropped from the binarized structure was performed using MAVI.^[21] Since the stereological parameters depend significantly on the binarization threshold value, parameter intervals are quoted for the maximum allowable range of threshold values which yields a structure without 'free-floating' segments and in qualitative agreement with the structures shown in Figures 3(a) and 3(b).

Porosity

The porosity obtained from the stereological analysis of the binarized reconstructed sample is 76 ± 1 vol.-%. An independent estimate for this parameter can be obtained as follows: Since the residual Ag fraction in the nanoporous gold sample is 4 at.-%, dealloying removes 79.2 % of all the atoms from the crystal lattice of the $\text{Ag}_{80}\text{Au}_{20}$ master alloy. This would lead to a porosity of 79.2 vol.-% in the idealized case of a constant sample size. Using the procedures described in Ref.^[8] we found a macroscopic volume reduction of about 4 %, which decreases the pore volume while leaving the volume of solid phase invariant. Thus, the final porosity is estimated at 76 vol.-%. The good agreement of this estimate with the results of the stereological analysis suggests that the choice of the threshold value range was appropriate.

Ligament- and Pore Size Distributions

First estimates of characteristic pore- and ligament sizes are obtained from the mean chord lengths of their respective phases in the binarized structure. The values are 55 and 17 nm for pores and ligaments, respectively. For a more detailed picture, the pore and ligament sizes were quantified using granulometry.^[21,30] The pore or ligament space was completely filled by overlapping spheres of different sizes, and each voxel in the phase was assigned to the largest sphere in which it was contained. The resultant distributions of sphere radii for the pores and ligaments, which are shown in Figures 5(a) and 5(b) respectively, can therefore be interpreted as a volume-weighted local feature size. The granulometry distributions were approximated by Gaussians and the peak positions – 28 ± 8 and 16 ± 5 nm for pores and ligaments, respectively – taken as a measure of the mean pore and ligament radius. The interval is the variance of the Gaussian fit. Simple structural models for porous materials^[31] can be used to relate these mean feature sizes to the volume fraction $q \approx (\text{ligament radius}/\text{pore radius})^2 = 0.32$. The reasonable agreement of the predictions of the simple structural models with the volume fraction of the reconstruction ($q = 0.24$), provides support for using these models to interpret general properties of nanoporous gold, such as mechanical behaviour.^[9,10]

Net Specific Surface Area

The net specific surface area (counting all surfaces irrespective of their orientation) per volume of the sample (pores and solid phase) is $a = 56 \pm 1/\mu\text{m}$. This is noticeably larger than what would be expected for an estimate based on the characteristic ligament size calculated above and on the pore fraction: long cylindrical objects of radius r packed at a volume fraction q have $a = 2q/r$. Using $q = 0.24$ and $r = 16$ nm we find $a = 30/\mu\text{m}$, only about half of the actual value. Similar discrepancies are common in structures with a wide distribution of feature sizes, in particular when the different mea-

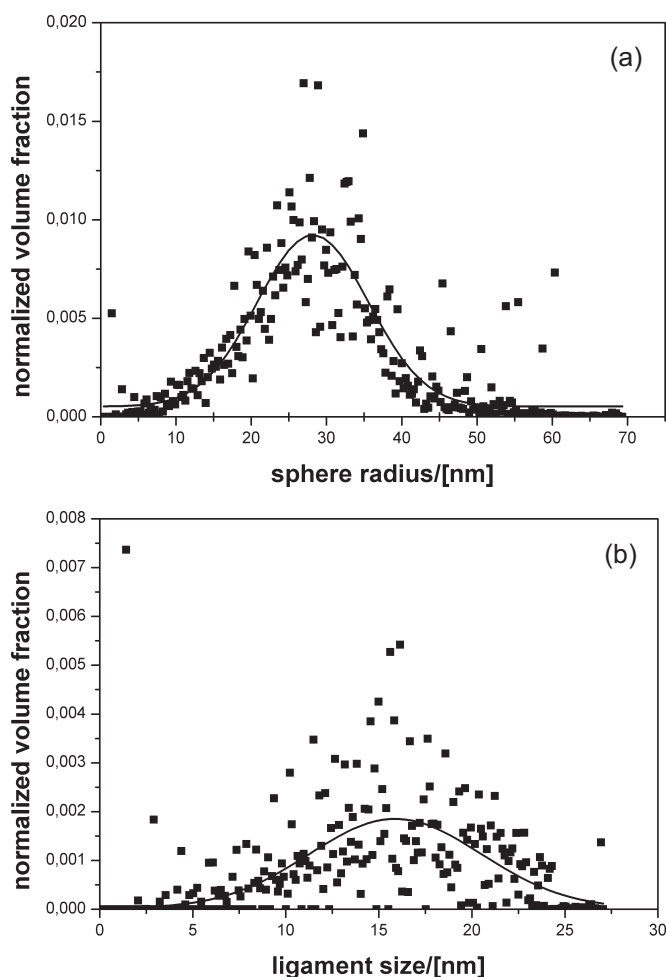


Fig. 5. a) Quantification of the pore sizes in terms of granulometry distribution as described in the text. [21] The solid line shows a Gaussian fit centred at a pore radius of 28 nm. b) Ligament size distribution as described in main text. Solid line shows a Gaussian fit, ignoring the data point at size < 2 nm. This fit reveals a mean ligament size of 16 nm.

sures for the size are based on different moments of the distributions. They emphasize the danger in using a single measure of size for characterizing the structure, and the need for a more differentiated analysis such as the one presented here.

Surface Orientation Distribution

The surface orientation distribution function $S_V(\mathbf{n})$ provides one of several measures for microstructural anisotropy. [22,32] In a sample with the volume V , the total area of surface with its normal oriented within the solid angle $d\omega$ about the unit vector \mathbf{n} is $S_V(\mathbf{n}) V d\omega$. MAVI [21] computes S_V by analysing a transform of the original binary image, which is obtained by labelling each voxel according to the occupancy (solid or pore) of the neighbouring voxels. Associated with the elements of the discrete set of possible neighbourhood configurations are 26 discrete surface orientations, with \mathbf{n} along the edges, face- and space diagonals of a voxel. [22] We present here the values of S_V for three orthogonal directions, namely the set of voxel edges x and y (in the plane of the foil)

as well as z (out of plane). The respective values are $S_x = 3.9 \mu\text{m}^{-1}\text{sr}^{-1}$, $S_y = 6.3 \mu\text{m}^{-1}\text{sr}^{-1}$, $S_z = 0.9 \mu\text{m}^{-1}\text{sr}^{-1}$. While the uncertainty in this data is unknown, the trend agrees with what can be seen in Figures 4: many ligaments appear elliptical in cross-section, with the long axis of the ellipse aligned preferentially with the sample (foil-) normal. Thus, surface orientations with their normal in the plane of the foil may be noticeably more frequent than those with a perpendicular orientation. The anisotropy may relate to the corrosion direction, which is presumably normal to the surface. However, we cannot exclude that the anisotropy develops during coarsening, which may also be influenced by the presence of the macroscopic sample surface.

The net specific surface area (per volume of the ligaments) governs the surface-induced pressure. [33] When the surface orientation distribution function is anisotropic, then the volumetric mean of the stress tensor is anisotropic. [33] Assuming a uniform and isotropic surface stress, the volumetric mean of the surface-induced stress is here expected to be largest in the direction normal to the foil.

Mean Curvature

The local value of the mean curvature, κ , (half the sum of the inverse values of the principal radii) at a given point on the surface is an important parameter, since gradients in κ provide driving forces for transport of matter that leads to coarsening. The mean curvature is also important for the local value of the normal component of the surface-induced stress underneath the surface of the ligaments. [34] The analysis provided an average value, $\langle\kappa\rangle$, of the mean curvature, defined as the integral of κ over the surface, divided by the total surface area, $\langle\kappa\rangle = 55 \mu\text{m}^{-1}$. The surface normal was oriented outwards as seen from the solid phase. Although it is dangerous to reduce the complicated microstructure to simple geometrical shapes, it may be instructive to compare the experimental value of $\langle\kappa\rangle$ with that of idealized, cylindrical ligaments of radius $r = 16 \text{ nm}$ (which is the measure for the mean ligament size deduced from Figure 5(b)): Such cylinders would come along with a value of $\kappa = 31 \mu\text{m}^{-1}$, similar in magnitude but noticeably smaller than the actual value. The comparatively large value of $\langle\kappa\rangle$ is again compatible with the existence of many small ligaments within the wide size distribution. Furthermore, the positive sign of $\langle\kappa\rangle$ suggests that – although there are many saddle-point like features where the principal radii of curvature are of opposite sign – the solid phase has essentially a convex surface. This contrasts with findings for bi-continuous structures formed by spinodal decomposition, which indicate a value of $\langle\kappa\rangle$ near to zero. [35] On average, compressive normal stresses are expected near the surface of our sample if the surface stress is positive.

Conclusion

This study highlights the potential of tomographic reconstruction from transmission electron microscopy images to characterize the microstructure of complex metal samples at

the nanoscale. The reconstruction allows visualization of the shape and size of the microstructural elements as well as their topology in 3-D. The technique appears particularly powerful when combined with 3-D stereological analysis. In this way, quantitative information may be obtained for various microstructural parameters (for instance, volume fraction of the phases, feature size distributions, and specific surface area) that control the material's performance in various applications. Similar approaches are emerging in other areas of science, for instance in soft condensed matter.^[36]

In addition, we present microstructural information for a material – nanoporous gold – which is under investigation for various applications, and for which the small feature sizes prevent characterisation using many established techniques, such as optical microscopy serial sectioning or x-ray tomography. The most important observations obtained using TEM tomography are: *i)* The structure represents a contiguous network of branched ligaments. *ii)* The structure is quite inhomogeneous, with a broad distribution of ligament and pore diameters and shapes. *iii)* As a consequence, the specific surface area is larger than what would be estimated based on the characteristic ligaments size. *iv)* In spite of the many saddle-points like features, the average mean curvature is positive and close to what would be expected for convex objects of the size corresponding to the ligament diameter. *v)* Encased voids are observed within the ligaments; there is no obvious explanation for the formation of these features.

We believe that this information contributes to establishing a basic description of the topology and local structure of nanoporous metals prepared by dealloying, which may form the basis for future models leading to a predictive understanding of their properties, such as strength, surface induced strain, or transport properties.

Received: February 23, 2007

Final version: April 18, 2007

Published online: June 14, 2007

- [1] G. Tammann, *Z. Anorg. Allg. Chem.* **1919**, 107, 1.
- [2] A. J. Forty, P. Durkin, *Philos. Mag. A* **1980**, 42, 295.
- [3] R. C. Newman, S. G. Corcoran, J. Erlebacher, M. J. Aziz, K. Sieradzki, *MRS Bull.* **1999**, 24, 24.
- [4] J. Erlebacher, M. J. Aziz, A. Karma, N. Dimitrov, K. Sieradzki, *Nature* **2001**, 410, 450.
- [5] R. W. Ertenberg, B. Andraka, Y. Takano, *Phys. B* **2000**, 284–288, 2022.
- [6] Y. Ding, M. W. Chen, J. Erlebacher, *J. Am. Chem. Soc.* **2000**, 126, 6876.
- [7] D. Kramer, R. N. Viswanath, J. Weissmüller, *Nano Lett.* **2004**, 4, 793.
- [8] S. Parida, D. Kramer, C. A. Volkert, H. Rösner, J. Erlebacher, J. Weissmüller, *Phys. Rev. Lett.* **2006**, 97, 035504.
- [9] J. Biener, A. M. Hodge, A. V. Hamza, *Appl. Phys. Lett.* **2005**, 87, 121908.
- [10] C. A. Volkert, E. T. Lilleodden, D. Kramer, J. Weissmüller, *Appl. Phys. Lett.* **2006**, 89, 061920.
- [11] A. J. Koster, U. Ziese, A. J. Verkleij, A. H. Janssen, K. P. De Jong, *J. Phys. Chem. B* **2000**, 104, 9368.
- [12] C. Kübel, A. Voigt, R. Schoenmakers, M. Otten, D. Su, T.-C. Lee, A. Carlsson, J. Bradley, *Micros. Microanal.* **2005**, 11, 378.
- [13] K. P. De Jong, A. J. Koster, *Chem. Phys. Chem.* **2002**, 3, 776.
- [14] H. Friedrich, M. R. McCartney, P. R. Buseck, *Ultramicrosc.* **2005**, 106, 19.
- [15] I. Arslan, T. J. V. Yates, N. D. Browning, P. A. Midgley, *Science* **2005**, 309, 2195.
- [16] P. A. Midgley, M. Weyland, J. M. Thomas, B. F. G. Johnson, *Chem. Comm.* **2001**, 10, 907.
- [17] P. A. Midgley, M. Weyland, *Ultramicrosc.* **2003**, 96, 413.
- [18] M. W. Anderson, T. Ohsuna, Y. Sakamoto, Z. Liu, A. Carlsson, O. Terasaki, *Chem. Comm.* **2004**, 8, 907.
- [19] M. Weyland, T. J. V. Yates, R. E. Dunin-Borkowski, L. Laffont, P. A. Midgley, *Scr. Mater.* **2006**, 55, 29.
- [20] Y. Ding, Y.-J. Kim, J. Erlebacher, *Adv. Mater.* **2004**, 16, 1897.
- [21] <http://www.itwm.fhg.de/mab/projects/MAVI/>.
- [22] J. Ohser, F. Mücklich, *Statistical Analysis of Microstructures in Materials Science*, John Wiley & Sons, Chichester **2000**, Chapters 3–4.
- [23] P. Gilbert, *J. Theor. Biol.* **1972**, 36, 105.
- [24] S. Parida, D. Kramer, J. Weissmüller, *unpublished data*.
- [25] A. M. Hodge, J. Biener, L. L. Hsiung, Y. M. Wang, A. V. Hamza, J. H. Satcher, *J. Mater. Res.* **2005**, 20, 554.
- [26] D. Lee, X. Wei, X. Chen, M. Zhao, S. C. Jun, J. Hone, E. G. Herbert, W. C. Oliverd, J. W. Kysar, *Scripta Mater.* **2007**, 6, 437.
- [27] G. Mason, *J. Colloid. Interface Sci.* **1970**, 32, 172.
- [28] A. V. Vvedenskii, I. K. Marshakov, *Russ. J. Electrochem.* **1995**, 31, 234.
- [29] E. Schofield, *Trans. Inst. Met. Finish.* **2005**, 83, 35.
- [30] P. Soille, *Morphological Image Anal.* Springer, Berlin **1999**.
- [31] L. J. Gibson, M. F. Ashby, in *Cellul. Solids: Struct. and Properties*, Pergamon, Oxford **1988**.
- [32] J. E. Hilliard, *Trans. AIME* **1962**, 224, 1201.
- [33] J. Weissmüller, J. W. Cahn, *Acta Mater.* **1997**, 45, 1899.
- [34] M. E. Gurtin, *Arch. Rat. Mech. Anal.* **1995**, 131, 67.
- [35] H. Jinnai, T. Koga, Y. Nishikawa, T. Hashimoto, S. T. Hide, *Phys. Rev. Lett.* **1997**, 78, 2248.
- [36] T. Hashimoto, H. Jinnai, Y. Nishikawa, T. Koga, *Macromol. Symp.* **2002**, 190, 9.